Sub-barrier fusion of stable and unstable nuclei with a microscopic interaction and Skyrme-Hartree-Fock densities

M. Rashdan
Islamic University, Faculty of Science, Physics Department, Madinah, Saudi Arabia
(Received 5 January 2013; revised manuscript received 9 June 2013; published 27 August 2013)

The fusion cross sections, barrier, and spin distributions of stable and unstable nuclei are investigated through a coupled-channel approach using a density and energy-dependent effective Brueckner G-matrix interaction. Calculations are carried out for the fusion reactions ^{16,18,20,22,24}O + ^{58}Ni and ^{28}Si + ^{58,62,64}Ni. Microscopic Skyrme-Hartree-Fock proton and neutron density distributions are used in the calculations. It is found that the energy dependence of the interaction potential enhances the fusion cross section, where it increases with increasing energy due to the decrease in the interaction barrier. The density dependence of the interaction is found to be of great importance, especially for unstable nuclei, since it directly relates the fusion cross section with the nuclear structure. The effect of the neutron skin is found to largely increase the fusion cross section and spin distribution due to the increase in the overlap region. The coupling to the inelastic excited states strongly enhances the fusion cross sections. The effect of the difference between the nuclear and charge deformations is also investigated.

DOI: 10.1103/PhysRevC.88.024615 PACS number(s): 24.10.Eq, 21.30.Fe, 25.70.Jj, 21.10.Ft

I. INTRODUCTION

The study of the structure and reactions of stable and unstable nuclei is one of the interesting aspects of nuclear theory. Nuclei near the neutron or proton drip lines are expected to have unusual extended density distributions or halo structures, which are expected to influence the scattering, reactions, and fusion cross sections of the colliding nuclei [1–18].

Many different mechanisms have been discussed for the description of sub-barrier fusion reactions as coupling to the low-energy excited states, nucleons transfer, deformation of ions, or neck formation during barrier penetration. Fusion cross sections are strongly enhanced at energies below the barrier by the coupling to both the low-energy surface vibrational states and the few-nucleon transfer channels [17,18].

The main part in calculating the cross section for a heavy-ion fusion reaction is the nucleus-nucleus interaction potential. The total interaction potential is the sum of the long-range repulsive force and the short-range nuclear attractive force. The Coulomb part of the interaction potential is well known, whereas the nuclear part is not clearly understood. Many concepts have been put forward to give a simple form of the nuclear potential. Among such concepts, proximity potential is well known for its simplicity and numerous applications in different fields. For example, a detailed study of the isotopic dependence of fusion dynamics was made in [19,20] using proximity potentials and a one-dimensional potential model. Similar calculations were carried out in [21] using proximity potentials as well as other different phenomenological potentials, such as the Akyuz-Winther [22,23], KNS [24], and Bass [25] potentials. However, a one-dimensional potential model was found to underestimate the fusion cross sections at lower energies. Moreover, proximity potentials are not unique, and they do not depend explicitly on the structure of the colliding nuclei.

The aim of this work is to investigate fusion reactions of stable and unstable nuclei through a microscopic density and energy-dependent nucleon-nucleon interaction, where the energy-density functional of the interacting nuclei is derived from effective Brueckner G-matrix interaction, which is the solution of the Bethe-Goldstone equation [26]. The energy density is an explicit functional of the proton and neutron density distributions, which is very important in describing and extracting information about the structure of stable and unstable nuclei. The effects of the coupling on the low-lying inelastic excitations are taken into account through the coupled-channels CCFULL code [27]. The proton and neutron density distributions of target and projectile are calculated from Skyrme-Hartree-Fock (SHF) calculations adopting the SKRA interaction [28]. Section II presents the theoretical description; calculations are presented and discussed in Sec. III. Summary and conclusions are presented in Sec. IV.

II. THEORETICAL DESCRIPTION

The interaction potential between two colliding nuclei separated by a distance R can be written as [26]

$$V(R;K_r) = E(R;K_r) - E(\infty;K_r), \tag{1}$$

where

$$K_r = \sqrt{\frac{2m}{\hbar^2}\frac{E_{\rm lab}}{A_P}} \tag{2}$$

is the relative momentum per nucleon. The relation between the laboratory and c.m. energies is

$$E_{\rm lab} = \frac{A_T + A_P}{A_T} E_{\rm c.m.}, \tag{3}$$

where A_P and A_T are the projectile and target mass numbers. The interaction potential $V(R;K_r)$ can be calculated as a function of K_r or $E_{\rm lab}$ or $E_{\rm c.m.}$ using relations (2) and (3). The total energy of the system, E, is obtained from the energy-density functional H through the relation

$$E(R;K_r) = \int d^3r H(\mathbf{r},R;K_r), \tag{4}$$

where

$$H(\mathbf{r}, R; Kr) = \tau(\rho_P, \rho_T; Kr) + \Pi(\rho_P, \rho_T; Kr) + H_{\rm cor}(\rho_p, \rho_n), \quad (5)$$

where ρ_P and ρ_T are the projectile and target densities. The first term in Eq. (5) is the kinetic energy density, which is calculated, in momentum space, from [26]

$$\tau(\rho_P, \rho_T; K_r) = \frac{\hbar^2}{2m}\left[\tau^{(2)} + K_G^2\rho\right], \quad (6)$$

$$\tau^{(2)} = \frac{\hbar^2}{2m} g \int_F \frac{d^3k}{(2\pi)^3}(k - K_G)^2, \quad (7)$$

where g is a spin-isospin degeneracy factor and K_G is a reference c.m. momentum ($K_G = \frac{\rho_P}{\rho} K_r$, where ρ is the total density of the system). $\int_F$ stands for the integration over the occupied states for two colliding nuclear matters. A surface correction term is added to the intrinsic kinetic energy density $\tau^{(2)}$ of the form

$$\delta\tau^{(2)} = \lambda|\nabla(\rho)|^2/\rho, \quad (8)$$

where the parameter λ takes values between $1/36$ and $9/36$ [29]. In this work, we consider $\lambda = 1.8/36$.

The second term in Eq. (5) is the potential energy density $\Pi(\rho_P, \rho_T; K_r)$, which is calculated, also in momentum space, from the G matrix [26],

$$\Pi(\rho_P, \rho_T; K_r) = \frac{1}{2}\sum_{\rm spin}\sum_{\rm isospin}\int_F \frac{d^3k}{(2\pi)^3}\int_F \frac{d^3k'}{(2\pi)^3}\langle kk'|G|kk'\rangle_a. \quad (9)$$

The reaction matrix G is the solution of the Bethe-Goldstone equation,

$$G(W) = \mathrm{V} + \mathrm{V}\frac{Q}{W - H_0 + i\epsilon}G(W), \quad (10)$$

where W is the starting energy and Q is the Pauli projection operator restricting the two nucleon intermediate states to be outside the Fermi sea. V denotes the bare nucleon-nucleon interaction taken to be the Reid soft core potential. This equation is solved in the momentum space configuration of two colliding nuclear matters (two Fermi spheres), using the generalized local density approximation [26].

The single-particle Hamiltonian H_0, when acting on a two-nucleon state, gives

$$H_0|\mathbf{k}\mathbf{k}'\rangle = (\varepsilon(\mathbf{k}) + \varepsilon(\mathbf{k}'))|kk'\rangle, \quad (11)$$

where the single-particle energies $\varepsilon(\mathbf{k})$ and $\varepsilon(\mathbf{k}')$, including both the kinetic energy and the real part of the single-particle potential $U(\mathbf{k})$, which is calculated from the reaction matrix G,

$$U(\mathbf{k}) = \frac{1}{4}\sum_{\rm spin}\sum_{\rm isospin}\int_F \frac{d^3k'}{(2\pi)^3}\langle \mathbf{k}\mathbf{k}'|G(W = \varepsilon(\mathbf{k}) + \varepsilon(\mathbf{k}'))|\mathbf{k}\mathbf{k}'\rangle_a. \quad (12)$$

The last term in Eq. (5) is a correction term due to three-body, relativistic, and symmetry energy corrections.

$$H_{\rm cor}(\rho_p, \rho_n) = \delta H_{3-\rm body}(\rho) + \delta H_{\rm rel}(\rho) + H_{\rm sym}(\rho, \beta). \quad (13)$$

The three-body and relativistic corrections were added in [28] in order to get the correct saturation properties of nuclear matter,

$$\delta H_{3-\rm body}(\rho) \simeq -2.4\rho\left(\frac{\rho}{\rho_{nm}}\right)^{1.1}, \quad (14)$$

$$\delta H_{\rm rel}(\rho) \simeq 2.4\rho\left(\frac{\rho}{\rho_{nm}}\right)^{8/3}, \quad (15)$$

where $\rho_{nm} = 0.17$ fm^{-3}.

For the symmetry energy coefficient we used a more realistic expression that is derived from Brueckner-Hartree-Fock (BHF) calculations of asymmetric nuclear matter, where the symmetry energy per particle can be written as [30]

$$H_{\rm sym}(\rho, \beta) = h_{\rm sym}(\rho)\beta^2, \quad \beta = (\rho_n - \rho_p)/\rho, \quad (16)$$

where $h_{\rm sym}(\rho = \rho_n + \rho_p)$ for $\rho \leqslant 0.5$ fm^{-3} is parametrized by the expression

$$h_{\rm sym} = \begin{cases} 278\rho - 643\rho^2 & \text{for } \rho \leqslant 0.1 \text{ fm}^{-3}, \\ 11.1 + 116.7\rho - 82.43\rho^2 & \text{for } 0.1 < \rho \leqslant 0.5 \text{ fm}^{-3}, \end{cases} \quad (17)$$

where the proton and neutron densities of the combined system are given by the sum of target and projectile densities, i.e.,

$$\rho_{p,n} = \rho^T_{p,n}(\mathbf{r}) + \rho^P_{p,n}(\mathbf{r} - \mathbf{R}). \quad (18)$$

III. NUMERICAL CALCULATIONS AND DISCUSSION

The proton and neutron density distributions of target and projectile are calculated from Skyrme-Hartree-Fock calculations using the Skyrme interaction SKRA [28]. This interaction was designed to describe both finite nuclei and nuclear matter

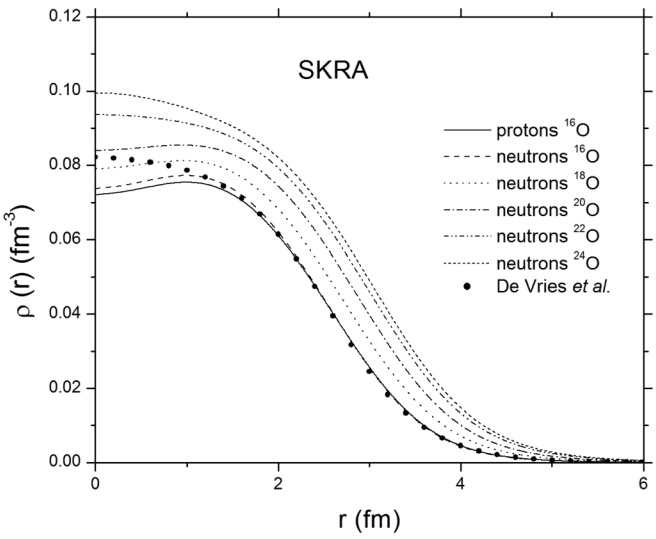

FIG. 1. Proton density distribution of ^{16}O and neutron densities of $^{16-24}$O calculated from SHF approach using SKRA interaction. The bold dots show the experimental density taken from De Vries *et al.* [31].

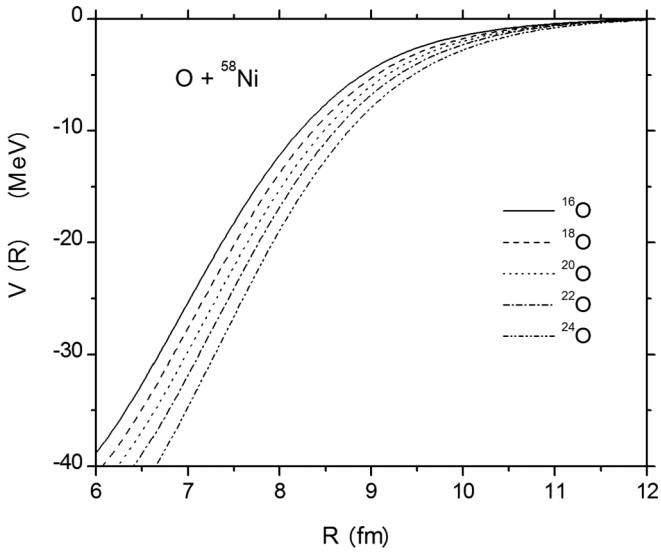

FIG. 2. Interaction potentials for $^{16-24}$O + ^{58}Ni against separation distance R derived from the G-matrix effective interaction and SHF densities at energies corresponding to the fusion barrier.

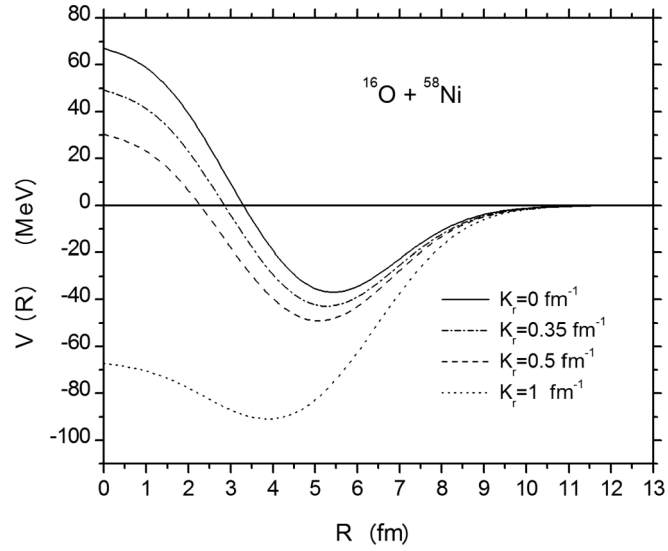

FIG. 3. Potentials calculated from G matrix, ^{16}O + ^{58}Ni, are plotted at different values of the relative momentum per nucleon $K_r = 0, 0.35, 0.5, 1$ fm^{-1}.

saturation, as derived from BHF calculations that include corrections due to many-body and relativistic effects [28].

Figure 1 shows the proton density distribution of ^{16}O, and the neutron densities of $^{16-24}$O, as calculated from the SHF calculation, using the SKRA interaction. As shown from this figure, the SHF proton density well fit the experimental one [31] in the surface and tail regions, which are the most important regions for scattering and fusion reactions. The nucleus ^{24}O is found to be a doubly-magic nucleus in the present approach, and this agrees with experiment [32]. Figure 1 shows also that when the neutron number increases, the neutron density increases. This causes a neutron skin, which is expected to increase the interaction potential, especially in the surface and tail regions.

Figure 2 shows the real part of the G-matrix interaction potential of $^{16-24}$O + ^{58}Ni against the separation distance R calculated using SHF densities, using the SKRA interaction, at energies corresponding to the interaction barrier. As shown in this figure at the surface and tail regions, the nuclear potential becomes deeper and more extended to larger distances when the neutron number is increased. This is because the interaction region is increased by increasing the neutron number due to the increases in the neutron density, as shown in Fig. 1. The neutron skin, appearing in the neutron density of ^{24}O, increases the nuclear potential in the surface and tail regions, as shown in Fig. 2. The increase in the nuclear potential around the barrier is expected to reduce the fusion barrier height and thus to enhance the fusion cross section. Figure 3 shows the energy dependence of the interaction potential where at low and intermediate energies, the potential becomes deeper with increasing energy, due to the decrease in the Pauli blocking effects with increasing energy.

We studied the energy dependence of fusion cross sections, spin, and barrier distributions calculated using the G-matrix interaction potential. We found that the energy dependence of the interaction potential affects the fusion cross section where it is enhanced with increasing energy, due to the decrease in the interaction barrier with increasing energy. We also found that around the barrier, the potential calculated at the incident center-of-mass energy equals the potential barrier predicted the same results for the fusion cross section and the barrier distribution as those calculated at each incident energy. Thus it is a very good approximation to use in fusion reactions around the barrier potentials which are calculated at the incident c.m. energy equaling the interaction barrier. This approximation will be used in all our calculations.

Table I presents the fusion barrier heights V_B and position R_B calculated using the G-matrix potential in a comparison

TABLE I. Fusion barrier heights V^B (MeV) and position R^B (fm) using G-matrix (present work), Akyuz-Winther (AW) [22,23] and KNS [24] interactions with empirical values [33,34].

Reaction	V_G	R_G	$V_{\rm KNS}$	$R_{\rm KNS}$	$V_{\rm AW}$	$R_{\rm AW}$	$V_{\rm emp}$	$R_{\rm emp}$
^{16}O + ^{58}Ni	32.21	9.3	31.14	9.48	31.78	9.45	31.67	9.3
^{18}O + ^{58}Ni	31.56	9.5	30.63	9.65	31.25	9.62		
^{20}O + ^{58}Ni	31.11	9.61	30.25	9.76	30.78	9.77		
^{28}Si + ^{58}Ni	54.7	9.5	52.6	9.82	53.29	9.85	53.8 ± 0.8	9 ± 0.9
^{28}Si + ^{62}Ni	53.47	9.43	51.97	9.95	52.6	9.99	52.89	9.89
^{28}Si + ^{64}Ni	52.9	10	51.68	10.01	52.3	10.05	52.4 ± 1.1	9.2 ± 1

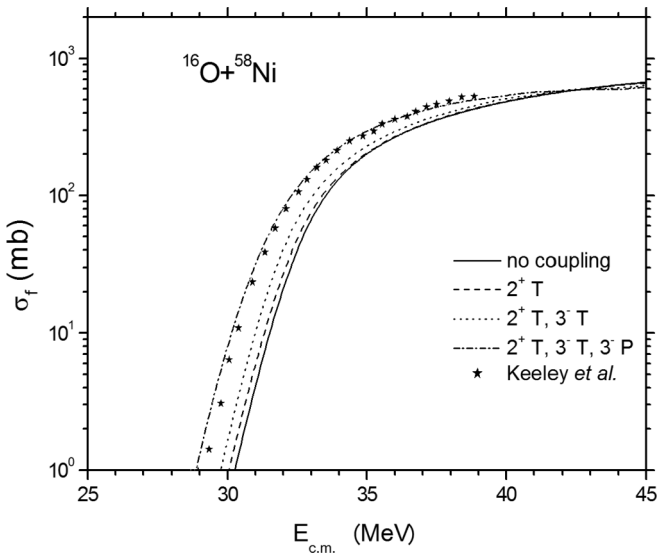

FIG. 4. Fusion cross section of ^{16}O + ^{58}Ni calculated using G-matrix potentials in the coupled channels using CCFULL code. The filled stars show the experimental data taken from Keeley *et al*. [37].

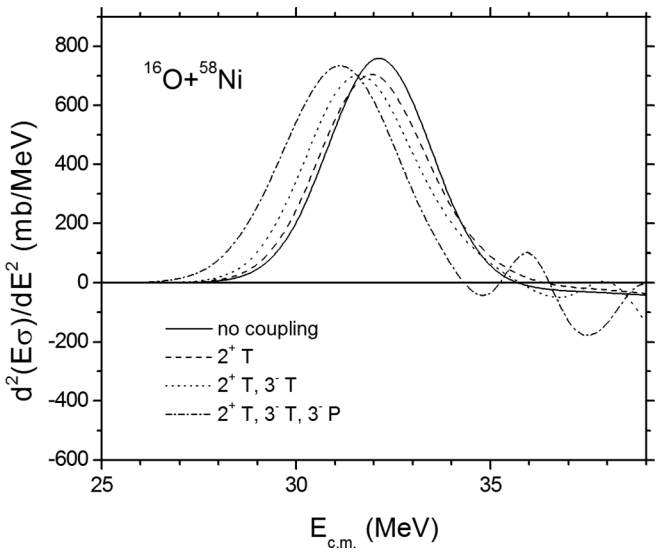

FIG. 6. Same as Fig. 4 but for the barrier distribution.

with the popular phenomenological Akyuz-Winther [22,23] and KNS [24] potentials. The Akyuz-Winther potential is based on the proximity formalism and the fitting to the densities of a variety of stable nuclei. The last two columns give the empirical values [33,34]. As seen from this table, the barriers decrease and the positions increase with increasing neutron numbers, which are consistent with the phenomenological potentials and the empirical values. Also noticed is that the barriers and positions are reproduced well by the G-matrix interaction in comparison with the phenomenological and the empirical predictions.

Figures 4–6 show the fusion cross section, spin, and barrier distributions for ^{16}O + ^{58}Ni calculated using the G-matrix interaction potential taking into account the effect of the coupling to the inelastic vibrational excited states 2^+, $E_2 = 1.454$ MeV, $\beta_2 = 0.183$, and 3^-, $E_3 = 4.475$ MeV, $\beta_3 = 0.22$ of the target; and 2^+, $E_2 = 6.92$ MeV, $\beta_2 = 0.36$, and 3^-, $E_3 = 6.19$ MeV, $\beta_3 = 0.6$ of the projectile. All the data of the vibrational excited states are taken from [35,36]. The experimental data for the ^{16}O + ^{58}Ni fusion cross section are taken from [37]. The coupling to the inelastic vibrational excited states are calculated using the coupled-channels CCFULL program [27]. As shown from these figures, the coupling to the low-lying excited states of target and projectile enhanced the fusion cross section, especially below the barrier, in agreement with the experimental data. For the case of angular momentum distribution, Fig. 5 shows that the coupling to inelastic excited states of target and projectile increases the angular momentum. The barrier distribution is shifted to lower c.m. energies, where it increases at lower energies, while increasing the coupling to inelastic excitation, as shown in Fig. 6.

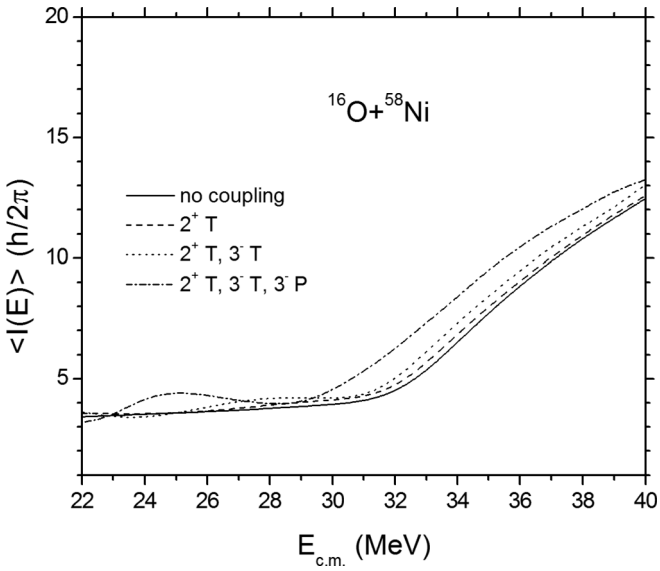

FIG. 5. Same as Fig. 4 but for the spin distribution.

Figure 7 shows the fusion cross section of ^{18}O + ^{58}Ni calculated using G-matrix interaction taken into account the effect of coupling to the 2^+ and 3^- of the target ^{58}Ni, and the 2^+, $E_2 = 1.982$ MeV, $\beta_2 = 0.355$ [35,36] (two-phonon) of the projectile ^{18}O. The experimental data for ^{18}O + ^{58}Ni fusion cross section are taken from [18,38,39]. As shown from Fig. 7, the experimental data are generally described by the interaction potential. However, the cross sections at lowest energies are not well described by the calculations. This could be due to the neutron transfer and/or the deformation of ^{18}O. Since the ^{18}O ground state exhibits an intrinsic deformation [40], one of the possible distortion effects is the alignment of deformed ^{18}O. The effect of the distortion of valence neutrons in ^{18}O has been investigated recently in [40]. They found that an analysis of the alignment effects and dipole polarization reveals that the alignment effect contributes significantly to the enhancement of the sub-barrier fusion cross sections.

Figures 8–10 show the cross sections and spin and barrier distributions, calculated for different projectile oxygen isotopes without including coupling to inelastic excitation. As shown from these figures, the fusion cross sections and spin and barrier distributions increase when increasing the

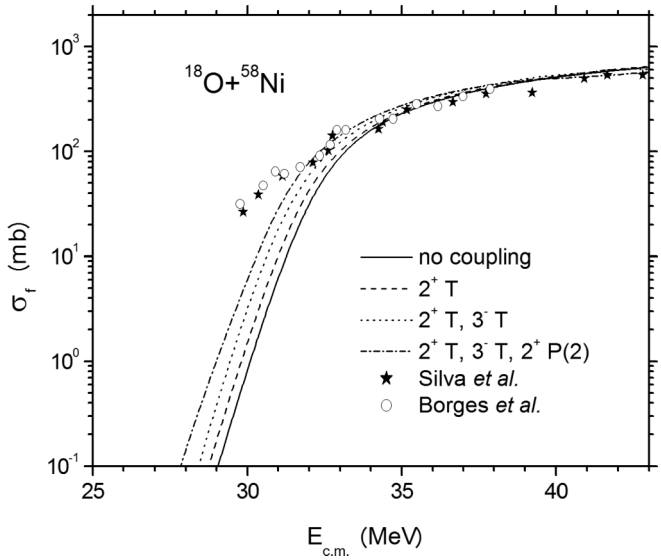

FIG. 7. Same as Fig. 4 but for ^{18}O + ^{58}Ni. The filled stars and open circles show the experimental fusion cross sections taken from Silva *et al*. [38] and Borges *et al*. [39].

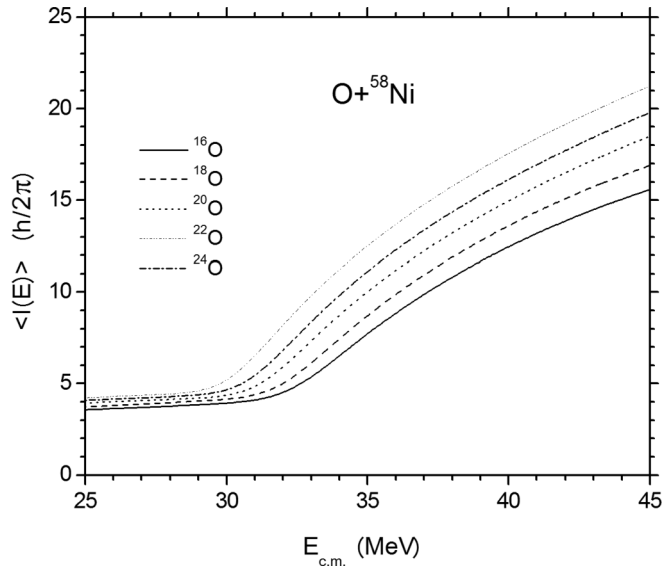

FIG. 9. Same as Fig. 8 but for the spin distributions.

neutron number. The heights of the barrier distributions also increase and shift to lower energies when increasing the neutron number. The larger increases are for ^{24}O, since it has the largest neutron skin. The reason for the increases in the cross sections and spin and barrier distributions when increasing the neutron number is that the negative nuclear potential increases with increasing neutron number, as shown in Fig. 2, which decreases the fusion barriers and thus enhances the probability of fusion. In fact, the increases in the negative nuclear potentials (in the surface and tail regions) are due to the increases in the neutron densities with increasing neutron number, as shown in Fig. 1. Hence, the present microscopic approach for calculating sub-barrier fusion directly relates the structure of nuclei with the fusion cross sections, which, on the other hand, is of great importance in extracting information about the structure of exotic nuclei.

Figure 11 shows the fusion cross section for ^{28}Si + ^{58}Ni calculated using the *G*-matrix interaction potential with SHF densities. The experimental data are taken from [34]. The experimental values of the deformation parameters of the 2^+ and 3^- vibrational states are taken from [35,36]. As shown in these figures, the experimental fusion cross sections are well described when the coupling to the low-energy 2^+ and 3^- surface excited states are considered with the two-neutron transfer channel, where the neutron transfer enhances the fusion cross section at lower energies ($Q_{2n} = -3.24$ MeV). The pair neutron transfer is considered in the CCFULL code by a phenomenological form factor which works well for negative Q values [27].

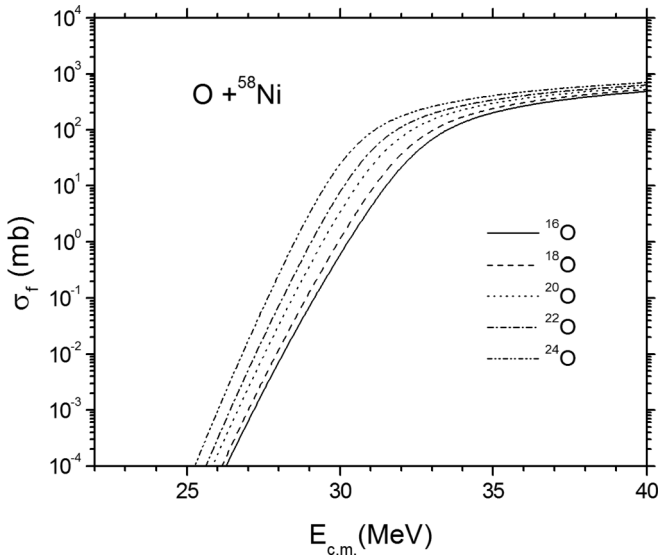

FIG. 8. Fusion cross sections of ^{16,18,20,22,24}O + ^{58}Ni calculated using *G*-matrix potentials without including coupling to inelastic excitation.

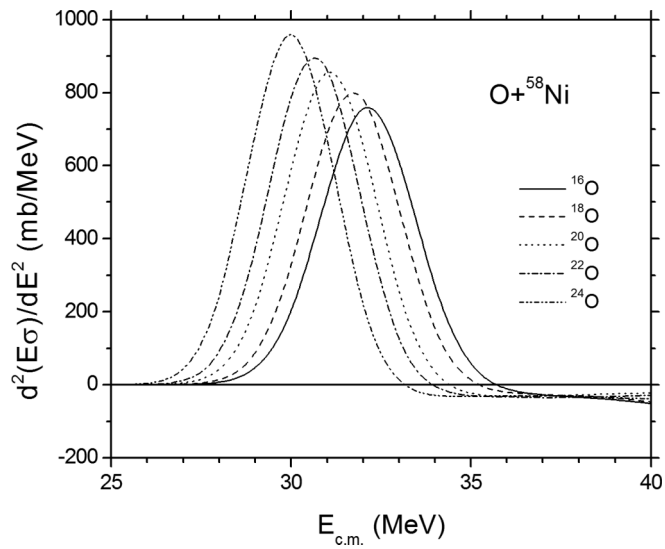

FIG. 10. Same as Fig. 8 but for the barrier distributions.

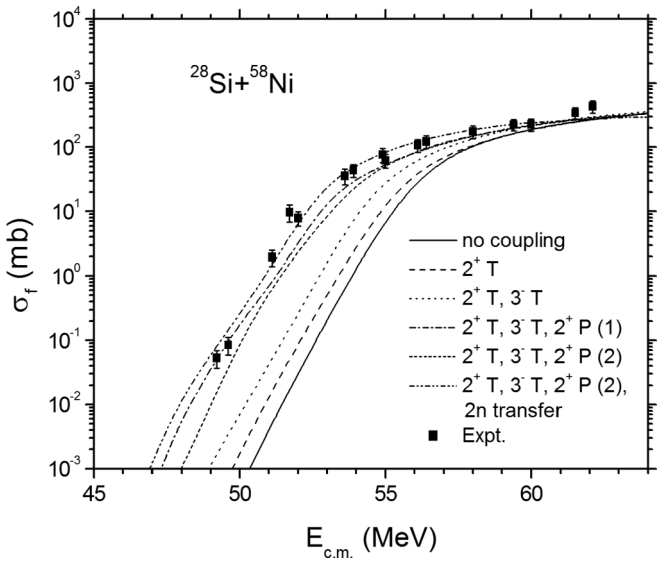

FIG. 11. Same as Fig. 4 but for ^{28}Si + ^{58}Ni.

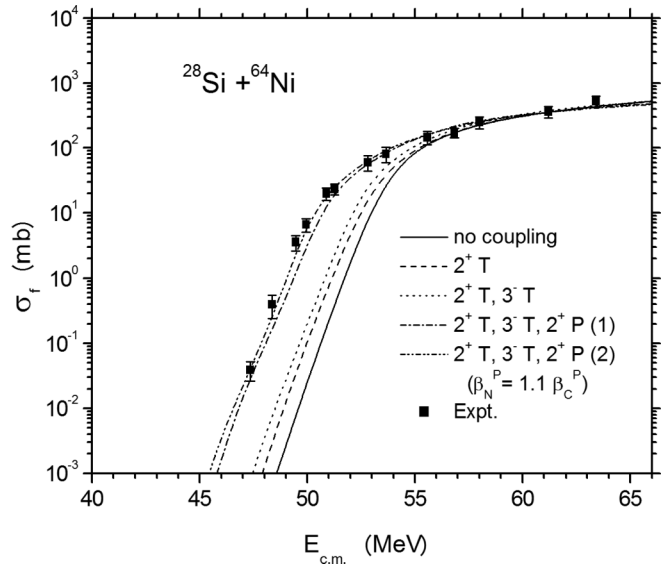

FIG. 13. Same as Fig. 4 but for ^{28}Si + ^{64}Ni.

Figure 12 shows the fusion cross section for ^{28}Si + ^{62}Ni calculated using a *G*-matrix interaction. The experimental data are taken from [34]. Figure 13 is the same as Fig. 12 but for ^{28}Si + ^{64}Ni. The experimental data are taken from [41]. The experimental values of the excitation energies and deformation parameters of the 2^+ and 3^- vibration states are taken from [35,36]. As shown in these figures, the experimental fusion cross sections are well described when the couplings to the low-energy 2^+ and 3^- surface excitation states are considered, especially for the reaction ^{28}Si + ^{62}Ni. For the case of ^{28}Si + ^{64}Ni, the calculated fusion cross section is slightly smaller than the data below the barrier after including the coupling to the inelastic excited states. Therefore, including the neutron transfer channels should enhance the fusion cross section below the barrier. However, the neutron transfer Q value for this reaction is positive and the CCFULL code probably does not work well for systems with positive Q values. In [18], the coupling to the low-energy surface oscillations during the fusion process have been considered in the simple CCFULL model, while the coupling to the transfer channels, with positive Q values, has been treated in the DWBA approximation. Recently, the effect of multineutron couplings has been considered through the NTFUS code for systems with large positive Q values, where a large enhancement of the fusion cross section below the barrier has been obtained that fairly describes the data [42]. However, as concluded in [42], it will be necessary to measure the neutron transfer cross sections to provide more information on the coupling strength of neutron transfer because its connection with fusion is not yet fully understood.

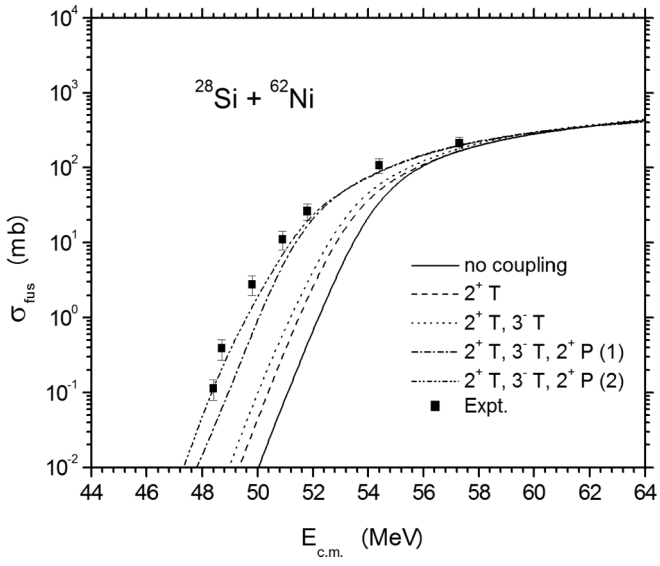

FIG. 12. Same as Fig. 4 but for ^{28}Si + ^{62}Ni.

On the other hand, different nuclear and Coulomb deformation parameters for the excited states, for nuclei with large positive Q values, could further increase the fusion cross section. We found that any increase in the nuclear deformation parameter other than the Coulomb one, enhanced the fusion cross section around and below the barrier. As a result, we considered $\beta_N^P \neq \beta_C^P$ for the reaction ^{28}Si + ^{64}Ni, where we took $\beta_N^P = 1.1\beta_C^P$. This slight increase in the nuclear deformation parameter fits the fusion cross section well, as shown in Fig. 13. This is consistent with [43], where they considered nuclear deformation β_{3n} about 1.5 of Coulomb deformation β_{3C} for the ^{19}F + ^{208}Pb fusion reaction.

IV. SUMMARY AND CONCLUSION

We have studied sub-barrier fusion reactions microscopically using a density- and energy-dependent effective *G*-matrix interaction and using Skyrme-Hartree-Fock densities. These interaction potentials are then used in a coupled-channels calculation for calculating the fusion reactions of the systems ^{16,18,20,22,24}O + ^{58}Ni and ^{28}Si + ^{58,62,64}Ni.

It was found that the energy dependence of the interaction enhances the fusion cross section due to the decrease in the

interaction barrier. The density dependence of the interaction is of great importance, since it directly relates the fusion cross sections with the structure of the interacting nuclei. The effect of neutron skin has been found to largely increase the fusion cross section and spin distribution, due to the increase in the overlap region with increasing neutron density. The coupling to the inelastic excited states enhanced the fusion cross section, as expected. The effect of the difference between the nuclear and charge deformations was investigated for the system ^{28}Si + ^{64}Ni, where the increase in the nuclear deformation parameter other than the Coulomb one enhanced the fusion cross section. The interaction potentials successfully described the barriers as well as fusion cross sections for the stable and unstable nuclei considered in this work.

[1] V. Scuderi *et al.*, Phys. Rev. C **84**, 064604 (2011).
[2] E. Crema, P. R. S. Gomes, and L. C. Chamon, Phys. Rev. C **75**, 037601 (2007).
[3] M. Notani, H. Esbensen, X. Fang, B. Bucher, P. Davies, C. L. Jiang, L. Lamm, C. J. Lin, C. Ma, E. Martin, K. E. Rehm, W. P. Tan, S. Thomas, X. D. Tang, and E. Brown, Phys. Rev. C **85**, 014607 (2012).
[4] T. Ichikawa, K. Hagino, and A. Iwamoto, Phys. Rev. Lett. **103**, 202701 (2009).
[5] A. S. Umar, V. E. Oberacker, and C. J. Horowitz, Phys. Rev. C **85**, 055801 (2012).
[6] H. Esbensen, Phys. Rev. C **85**, 064611 (2012).
[7] R. Wolski *et al.*, Eur. J. Phys. A **47**, 111 (2011).
[8] L. Canto, P. Gomes, R. Donangelo, and M. Hussein, Phys. Rep. **424**, 1 (2006).
[9] C. Bertulani, V. Flambaum, and V. Zelevinsky, J. Phys. G **34**, 2289 (2007).
[10] L. Canto, P. Gomes, J. Lubian, L. Chamon, and E. Crema, Nucl. Phys. A **821**, 51 (2009); J. Phys. G **36**, 015109 (2009).
[11] K. Tanaka *et al.*, Phys. Rev. Lett. **104**, 062701 (2010).
[12] D. Steppenbeck *et al.*, Phys. Rev. C **81**, 014305 (2010).
[13] M. Takechi *et al.*, Nucl. Phys. A **834**, 412 (2010).
[14] K. Hagino, A. Vitturi, C. H. Dasso, and S. M. Lenzi, Phys. Rev. C **61**, 037602 (2000).
[15] G. Ademard *et al.*, Phys. Rev. C **83**, 054619 (2011).
[16] J. Kolata *et al.*, Phys. Rev. Lett. **81**, 4580 (1998).
[17] C. J. Horowitz, D. K. Berry, and E. F. Brown, Phys. Rev. E **75**, 066101 (2007).
[18] V. Yu. Denisov, Eur. J. Phys. A **7**, 87 (2000).
[19] N. K. Dhiman and R. K. Puri, Acta Phys. Pol. B **37**, 1855 (2006).
[20] O. N. Ghodsi, R. Gharaei, and F. Lari, Phys. Rev. C **86**, 024615 (2012).
[21] O. N. Ghodsi and R. Gharaeia, Eur. J. Phys. A **48**, 21 (2012); I. Dutt and Rajeev K. Puri, Phys. Rev. C **81**, 064609 (2010); T. Ichikawa, K. Hagino, and A. Iwamoto, *ibid.* **75**, 064612 (2007).
[22] O. Akyuz and A. Winther, in *Proceedings of Enrico Fermi International School of Physics, Course LXXVII*, edited by R. A. Broglia, C. Dasso, and R. Richi (North- Holland, Amsterdam, 1981).
[23] R. A. Broglia and A. Winther, *Heavy Ion Reactions*, *Lecture Notes, Vol. I: The Elementary Processes* (Addison-Wesley, Reading, MA, 1991).
[24] H. J. Krappe, J. R. Nix, and A. J. Sierk, Phys. Rev. C **20**, 992 (1979).
[25] R. Bass, Phys. Rev. Lett. **39**, 45 (1977); in *Lecture Notes Phys.* Vol. 117 (Springer, Berlin, 1980), p. 281.
[26] M. Rashdan, Phys. Rev. C **56**, 1019 (1997); N. Ohtsuka, R. Linden, A. Faessler, and F. B. Malik, Nucl. Phys. A **465**, 550 (1987).
[27] K. Hagino, N. Rowley, and A. T. Kruppa, Comput. Phys. Commun. **123**, 143 (1999).
[28] M. Rashdan, Mod. Phys. Lett. A **15**, 1287 (2000).
[29] I. Dutt, Chin. Phys. Lett. 27, 112401 (2010).
[30] M. Rashdan, Phys. Scr. **68**, 166 (2003).
[31] H. De Vries, C. W. De Jager, and C. De Vries, At. Data Nucl. Data Tables **36**, 495 (1987).
[32] C. Hoffman, T. Baumann, D. Bazin, J. Brown, G. Christian, D. H. Denby, P. A. DeYoung, J. E. Finck, N. Frank, J. Hinnefeld, S. Mosby, W. A. Peters, W. F. Roger, A. Schiller, A. Spyrou, M. J. Scott, S. L. Tabor, M. Thoennessen, and P. Voss, Phys. Lett. B **672**, 17 (2009).
[33] J. O. Newton, R. D. Butt, M. Dasgupta, D. J. Hinde, I. I. Gontchar, C. R. Morton, and K. Hagino, Phys. Rev. C **70**, 024605 (2004).
[34] A. M. Stefanini *et al.*, Nucl. Phys. A **456**, 509 (1986).
[35] S. Raman, C. W. Nestor, Jr., and P. Tikkaneny, At. Data Nucl. Data Tables **78**, 1 (2001).
[36] T. Kibedi and R. H. Spear, At. Data Nucl. Data Tables **80**, 35 (2002).
[37] N. Keeley, J. S. Lilley, J. X. Wei *et al.*, Nucl. Phys. A **628**, 1 (1998).
[38] C. P. Silva, D. Pereira, L. C. Chamon, E. S. Rossi, Jr., G. Ramirez, A. M. Borges, and C. E. Aguiar, Phys. Rev. C **55**, 3155 (1997).
[39] A. M. Borges, C. P. da Silva, D. Pereira, L. C. Chamon, E. S. Rossi, Jr., and C. E. Aguiar, Phys. Rev. C **46**, 2360 (1992).
[40] Yasutaka Taniguchi, Yoshiko Kanada-En'yo, and Tadahiro Suhara, arXiv:1202.0632 [nucl-th].
[41] A. K. Sinha, L. T. Baby, N. Badiger *et al.*, J. Phys. G **23**, 1331 (1997).
[42] A. Richard, C. Beck, H. Q. Zhang, C. J. Lin, F. Yang, H. M. Jia, X. X. Xu, Z. D. Wu, F. Jia, S. T. Zhang, and Z. H. Liu, arXiv:1104.5333 [nucl-th].
[43] M. Ismail and M. Seif, Int. J. Mod. Phys. E **22**, 1350010 (2013).